Earth Planet. Sci. Lett. 649 (2025) 119095

Contents lists available at ScienceDirect

Earth and Planetary Science Letters

journal homepage: www.elsevier.com/locate/epsl

Lower mantle water distribution from *ab initio* proton diffusivity in bridgmanite

Chris E. Mohn [a,b,*], Razvan Caracas [a,c], Clinton P. Conrad [a]

[a] *Centre for Planetary Habitability (PHAB), University of Oslo, N-0315 Oslo, Norway*
[b] *Department of Chemistry and Center for Materials Science and Nanotechnology, University of Oslo, Oslo 0371, Norway*
[c] *Université Paris Cite, Institut de Physique du Globe de Paris, CNRS, Paris, France*

ARTICLE INFO

Editor: F.-Z. Teng

ABSTRACT

Proton self diffusion coefficients for bridgmanite at lower mantle conditions are calculated from *ab initio* molecular dynamics simulations. We find that the proton self diffusion coefficient, D^{self} is nearly constant $\sim 10^{-8}$ $\mathrm{m^2\,s^{-1}}$ along the lower mantle geotherm but increases by nearly one order of magnitude from $\sim 10^{-10}$ $\mathrm{m^2\,s^{-1}}$ to $\sim 10^{-9}$ $\mathrm{m^2\,s^{-1}}$ along a cold slab geotherm to about 1800 km depth. These rates imply that the proton diffusion length scale is less than 10 km in lower mantle peridotite in the 150-200 million years timescale for slab material to sink through the lower mantle. Cold wet slabs probably lose less than one percent of their total water content to the ambient mantle on their journey through the lower mantle, indicating that recycled water is far from homogeneously distributed since slab delivery is highly heterogeneous. We estimate that 0.1 to 0.3 ocean masses (<100 ppm wt%) of recycled water may be currently stored in slab remnant materials within the lower mantle. This water is likely not entrained by plumes but is instead captured by background mantle flow before returning to the mid-ocean ridges. By contrast, deep-rooted mantle plumes may entrain materials containing primordial-like water from the lowermost mantle or the core, and preserve these anomalies in fairly small-scale heterogeneities. Over the age of the Earth, the proton diffusion length scale is a few tens of km, which places constraints on the size of possible primordial water reservoirs isolated from convective mixing, and indicates little flux of water across the core-mantle boundary.

1. Introduction

Earth is a wet planet. Not only at its surface where clouds, oceans, rivers, glaciers and groundwater are involved in a planetary surface cycle, but also within its depths. A part of this deep water has been trapped somewhere inside the Earth's interior for billions of years, isolated from convective mixing. Evidence for deep primordial water is fingerprinted in many Ocean Island Basalts, OIBs, from Baffin Island for example, where measurements of unusually low deuterium-to-hydrogen ratios support the presence of isolated primitive reservoirs (Hallis et al. (2015); Li et al. (2022b)). In addition to these hidden primordial water sources, the deep Earth also contains a substantial amount of *recycled* water. Over 3-4 Gyr, weathering alteration and hydration processes have incorporated seawater into sedimentary rocks that have been carried by subducting slabs back into the Earth's deep interior (Crowley et al. (2011); Sandu et al. (2011); Korenaga (2011); Korenaga et al. (2017)).

The flux of water from the surface into the mantle is thought to be controlled by rates of subduction and slab temperatures, with slow and warm slabs losing most of their water to hydrous buoyant magmatism of the back-arc. Nevertheless, some slabs are cold and fast enough to escape the sub-volcanic dehydration front, and overall as much as 30% of subducted water is thought to reach the mantle transition zone (MTZ) (Rüpke et al. (2004); van Keken et al. (2011); Karlsen et al. (2019)). Evidence for a "wet" MTZ, at least locally, is supported by a spectroscopic analysis of ringwoodite with 1.5 wt% water in solid solution found inside a diamond (Pearson et al. (2014)). Although water is readily accommodated in MTZ minerals, with typical solubility ranging from 2 to 4%, the overall hydration state of the MTZ varies laterally (Peslier et al. (2017); Houser (2016)) because the slab-controlled delivery of water is highly heterogeneous. Some slabs may stagnate near the boundary between the MTZ and the lower mantle but they will eventually continue downwards into the lower mantle and bring water with them.

---

* Corresponding author.
E-mail address: chrism@geo.uio.no (C.E. Mohn).

https://doi.org/10.1016/j.epsl.2024.119095
Received 15 April 2024; Received in revised form 14 October 2024; Accepted 21 October 2024

Cold wet slabs penetrating into the lower mantle can possibly dehydrate at 700-800 km depths, following the transformation from wet ringwoodite to an assemblage of bridgmanite + (Mg,Fe)O magnesiowüstite + $CaSiO_3$ perovskite, and may continue to dehydrate down to about 1100 km below the surface due to the decomposition of hydrous phase D (Nishi et al. (2014); Panero and Caracas (2020)). Dehydration at these depths may be accompanied by $\sim$ 1% partial melting (Schmandt et al. (2014)) and water will probably, in part, be transported in buoyant fluids along fractures to shallower depths (Pearson et al. (2014); Walter (2021)). However, water in the migrating fluids may also "redissolve" into bridgmanite (bm) within the bulk of the slab or into the minerals of the former slab crust, for example silica, depending on composition, thermodynamic conditions, and texture (Walter (2021)).

The flux of water into the lower mantle from wet and cold sinking slabs depends on water solubility and hydrous inclusions within major slab crust and mantle minerals bridgmanite, ferropericlase, $CaSiO_3$, SiO_2, as well as partitioning of water/protons between MTZ and lower mantle minerals. Partitioning of water between ringwoodite and bridgmanite suggests that water prefers ringwoodite (Hernández et al. (2013)) but since bridgmanite is about 10 times more voluminous, it has the potential to hold a substantial amount of water driven by a net influx into dry bridgmanite, even if its water solubility may be lower (Kaminsky (2018)). This MTZ to lower mantle influx is also controlled by proton diffusivity in bridgmanite and proton solubility. The solubility of water in bridgmanite, however, ranges from *very dry* (<10 ppm) to *very wet* (> 10000 ppm) depending on experimental conditions and material compositions (such as Al and Fe contents) (Kaminsky (2018)). Bridgmanite in representative mantle pyrolite and peridotite (i.e. in $(Mg_{0.88}Fe^{3+}_{0.065}Fe^{2+}_{0.035})(Al_{0.14}Si_{0.90})O_3$ (Fu et al. (2019)), however, can typically dissolve 1000-2500 ppm of water (Litasov et al. (2003); Fu et al. (2019); Murakami et al. (2002)). Although Liu et al. (Liu et al. (2021)) argue that such a high water solubility in bridgmanite may be due to the presence of tiny hydrous inclusions in grains (Liu et al. (2021)), bridgmanite (Liu et al. (2021)) within slab lower mantle peridotite can still potentially carry with it a substantial amount of water (*i.e.* ~ 0.1 wt% or more) dissolved both into the crystal structure and incorporated in grain boundaries (Kaminsky (2018); Liu et al. (2021); Litasov et al. (2003); Murakami et al. (2002)).

If water can be carried all the way to the lowermost mantle, it can possibly react with iron-rich phases to form hydrated iron-oxides (Walter (2021); Mao et al. (2017)), which have the potential to impact the redox state of the entire Earth (Walter (2021); Mao et al. (2017)). The water might even migrate into Earth's metallic core due to the affinity of hydrogen for iron at high pressure (Ohtani and Zhao (2009); Kim et al. (2023)). For these reactions to occur, hydrated minerals must come into mechanical contact with the iron-rich phases of the core-mantle boundary (CMB) region, which are potentially confined to within a few km of the boundary itself (Yoshino (2019)). If the slab's water does not interact with iron in the CMB region, then it would remain dissolved in the slab's core (hydrated mineral) or crust (silica), where it would be carried away by the strong lateral flow in the direction of the LLSVPs (Ammann et al. (2010); Conrad et al. (2013); Heyn et al. (2020)). This water is then likely to be brought back to the upper mantle by hot upwellings (plumes or broad-scale flow), and eventually outgas at hotspots and mid-ocean ridges (completing a mantle water cycle).

Whether the hydrated bridgmanite interacts with the CMB or is advected across the lower mantle thus depends on the degree to which water (protons) can migrate away from the central core of the slab. To better understand the fate of the recycled water in the lower mantle, we constrain rates of proton self-diffusion in bridgmanite - the main lower mantle mineral - using *ab initio* molecular dynamics (MD) simulations. Knowledge of the rate of proton diffusivity in bridgmanite is essential for estimating the escape of water from the slabs, the flux of water between the wetter cold slabs and the ambient hot drier lower mantle, the rates of leakage of primordial-like water from heterogeneities entrained by deep-rooted mantle plumes, and the fluxes of water across the core-mantle boundary (CMB). Proton diffusivity estimates can also help to constrain the size of possible primordial water reservoirs in the lower mantle, which are intimately related to length scales of proton travel within bridgmanite on timescales of Earth's age. Moreover, understanding water cycling within the lower mantle is crucial for understanding Earth's water budget and storage distributions. Because mantle rheology is extremely sensitive to water content (Muir and Brodholt (2018)), changes in lower mantle water storage may ultimately dictate the dynamics and thermal history of the whole Earth (Crowley et al. (2011); Sandu et al. (2011); Korenaga (2011)).

2. Methodology

2.1. Hydrogen diffusion coefficients

Calculations of proton diffusion are carried out using first-principles molecular dynamics simulations. Since the protons jump rapidly between distinct residential interstitial sites, we can calculate the proton self-diffusion coefficient from a *hopping model* (Jacucci and Rahman (1978); Mohn et al. (2009a,b, 2021)), using

$$D^{\text{self}} = \frac{1}{6}\sum_i f_i \Gamma_i a_i^2, \tag{2.1}$$

where i refers to the jump directions, i.e. between nearest neighbor resident cavities aligned in the crystallographic $\langle 100\rangle$ direction, next-nearest neighbors aligned in the $\langle 110\rangle$ direction, or third-nearest neighbors aligned in the $\langle 111\rangle$ direction, etc. Γ_i and a_i are the jump frequency and the jump distance in direction i. Correlation factors, f_i, which measure the correlations between successive jumps of a proton, can be calculated using $f_i = 1 + 2\langle \cos\theta_{l,l+1}\rangle$, where $\theta_{l,l+1}$ is the angle between two consecutive jumps l and $l+1$. We count the number of hydrogen jumps in a MD simulation and record the jump frequency, the jump distance, and the angle, θ, between two consecutive jumps.

From the proton self-diffusion coefficient, we can calculate the flux of water over boundaries, such as the flux of water from a (wet) hydrated slab core to dry surrounding slab material and ambient mantle, by solving Fick's second law of non-steady-state diffusion. If we assume that the water is distributed homogeneously in the hydrated part of the slab with a constant concentration $c_S = c(x=0,t)$ at the boundary (i.e. at the hydrated slab core - dry slab interface), the water concentration, $C(x,t)$, at a distance x from the boundary at time t is given by:

$$C(x,t) = c_S \text{erfc}\left(\frac{x}{2\sqrt{(D^{\text{self}}t)}}\right), \tag{2.2}$$

where erfc is the complementary error function. The total loss of water at a given time t per unit surface area is found by integrating the concentration profile (Eq. (2.2)) from x = 0 to ∞. Total outflux at t for a body with volume V depends on it's slab surface-area to slab-volume ratio which is investigated here for different slab surface topographies.

The assumption that water is uniformly distributed within the hydrated portion of the slab warrants a few comments. In general water is probably not homogeneously distributed within the hydrated portion of the slab core but instead the distribution depends on a number of conditions, such as slab history and proton diffusivity at shallower depths, particularly during the passage through the MTZ. Typical values of D^{self} for protons in ringwoodite at 2500 K are between 1×10^{-10} m^2 s^{-1} and 1 $\times10^{-9}$ m^2 s^{-1} at around 2000 K and 25 GPa (Caracas and Panero (2017)) and the average traveling length for protons is therefore between a few hundred meters to about 1 km in $\sim$ 10-50 Myr representative time-scale for the slab residence time in the transition zone. This illustrates that proton diffusivity may not be sufficiently fast to entirely homogenize the hydrated core of the slab before entering the lower mantle. Estimations of water loss from water-saturated slab cores could therefore be slightly smaller than that calculated here, assuming a homogeneous distribution in Eq. (2.2). Moreover, interdiffusion of charged protons from Eq. (2.2) must be balanced by charge-compensating counter-fluxes of positively charged species or parallel fluxes of negatively charged species that have a similar or higher mobility than the protons themselves (Karato (2013); Kohlstedt and Mackwell (1998); Mackwell and Kohlstedt (1990)). Possible charge-compensating candidates in bridgmanite are oxygen vacancies, small-polarons, or electrons and holes, all which have high mobility. However, the concentration of vacancies in bridgmanite in lower mantle peridotite may be very low above 40 GPa (see e.g. Liu et al. (2017)), but since bridgmanite in peridotite contains 5-10% iron with $Fe^{3+}/(Fe^{2+}+Fe^{3+}) \sim 0.6$ (Frost et al. (2004); McCammon (1997); Mohn and Trønnes (2016)), high small-polaron carrier concentrations formed by Fe^{3+}/Fe^{2+} pairs accompanied by low activation barrier heights (i.e. $E_{\text{a, small polarons}} \approx< 0.5$ eV $\approx E_{\text{a, protons}}$ (Yoshino et al. (2016); Shankland et al. (1993)) suggests that small-polarons conductivity can act as counter fluxes to protons. This is consistent with experimental measurements of interdiffusion of protons in olivine where proton-fluxes are compensated by counter-fluxes of polarons or possibly electrons in bands (Kohlstedt et al. (1996); Mackwell and Kohlstedt (1990)).

2.2. Computational details

To calculate proton diffusion from MD simulations, we use the VASP package (Perdew et al. (1996); Kresse and Hafner (1993); Kresse and Joubert (1999)) with the Perdew–Burke–Ernzerhof functional (Perdew et al. (1996)), an energy cut-off of 400 eV for the electronic wave function and the gamma point only for sampling the Brillouin zone. Calculations of D^{self} using an energy cut-off of 500 eV and 600 eV carried out at 25 GPa and 2000 K were within the error bars of that calculated using an energy cut-off of 400 eV. To minimize self-interaction errors associated with Fe^{2+} $3d$ electrons, we use an on-site Hubbard $+U$ term of 4 eV for Fe^{2+} which is a typical average value used for studying iron-bearing $MgSiO_3$ (Hsu et al. (2012)).

The MD runs are carried out within the NVT ensemble, where the cell volume, V, is tuned during several short runs to match an average total pressure of 25, 50, 75, 100, and 125 GPa. The temperatures range between 1500 and 3000 K. We use a Nosé-Hoover thermostat and a step-length of 1 fs. Decreasing the step length to 0.1 fs had little effect on the calculated diffusion coefficient. All runs were carried out between 0.1 ns and 1.0 ns to collect sufficient statistics (i.e. at least 70 proton jumps were recorded at a given P, T condition, and in some runs, we counted more than 200 jumps). We find that f in Eq. (2.1) is between 0.9 and 1.0 suggesting that there is little correlation between successive proton jumps.

We employ bm supercells containing 81 atoms, constructed by doubling the conventional orthorhombic 20-atoms cell of perovskite-structured $MgSiO_3$ (bm) along the two crystallographic a and b directions. Muir and Brodholt (Muir and Brodholt (2018)) investigated different plausible mechanisms for the incorporation of water in bm, for example, by replacing Si^{4+} and Mg^{2+} with $4H^+$ or $2H^+$ atoms respectively, or replacing one Si^{4+} with one Al^{3+} and one H^+ to maintain overall charge neutrality. They found that the exchange of Si^{4+} with Al^{3+} + H^+ was the energetically most favorable mechanism, and the resulting composition is also fairly consistent with the aluminum content measured in bm in a peridotitic lithology (∼10 mole % aluminum). In this work, we investigate proton diffusion in Al-bearing bridgmanite where the simulation box has a composition consistent with the following compound: $MgSi_{0.9375}Al_{0.0625}(OH)_{0.0625}O_{2.875}$. For calculations carried out with Fe^{2+} the composition was: $Mg_{0.9375}Fe_{0.0625}Si_{0.9375}Al_{0.0625}(OH)_{0.0625}O_{2.9375}$. The solubility of water in bridgmanite (∼ 0.1-0.25 wt% H_2O in peridotitic or pyrolitic lithologies (Fu et al. (2019); Hernández et al. (2013); Litasov et al. (2003); Kaminsky (2018); Murakami et al. (2002))) is probably much lower than those within our 81-atom supercell. Anyhow this does not influence the calculated proton diffusivity (Eq. (2.1)), as long as correlations between protons across the boundary (proton self-interaction) are negligible. We check this from additional calculations of D^{self} carried out using a large simulations box containing 648 atoms. This cell was constructed by doubling the 81-atom cell in each crystallographic direction and has the same composition as that of the 81-atom cell. Results from these test calculations show that the diffusion coefficient determined using a 648-atom cell was in good agreement with that found using the 81-atom cell. For example, in the 648-atom simulation, we were able to record more than 100 proton jumps at 25 GPa and 2000 K in a ∼ 20 ps run. The calculated D^{self} from this run was 3.4×10^{-8} $m^2\ s^{-1}$, which is in good agreement with the value calculated using an 81-atom cell (2.8×10^{-8} $m^2\ s^{-1}$) and consistent with a cell-size convergence analysis of proton diffusivity in bridgmanite carried out using force field potentials (Peng and Deng (2024)).

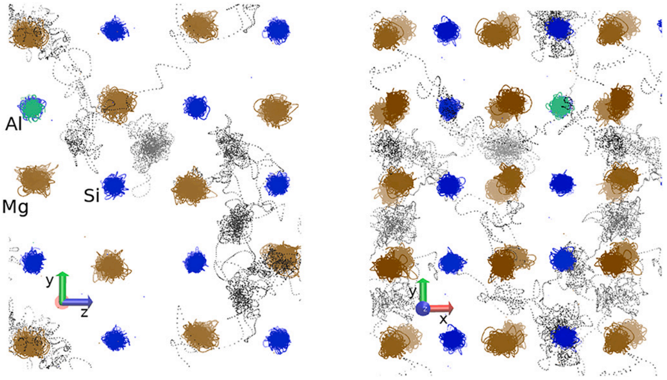

Fig. 1. Proton diffusion trajectory (black/gray dashed lines) from a 20 ps MD snapshot in Al-bearing bridgmanite at 2500 K and 50 GPa using an orthorhombic 81 atom simulation cell. Left and right figures are views of the same trajectory along the crystallographic x and z directions respectively. Blue, brown, and green lines represent Si, Mg, and Al respectively. The oxygen atoms are omitted for clarity. The trajectories are drawn using VMD (Humphrey et al. (1996)).

3. Results and discussion

3.1. Proton self-diffusion in bridgmanite

Atomistic trajectories extracted from the MD simulations show that protons vibrate near interstitial lattice positions with rapid jumps mainly between nearest neighboring interstitial positions. We count, for example, one proton jump between neighboring interstitial sites about every 5 ps for a hot mid-mantle geotherm and there is no strong preference for diffusion in a particular crystallographic direction. A typical trajectory of a single proton diffusing in Al-bearing bm at high temperature is shown in Fig. 1.

Fig. 2a shows the Arrhenius plots of proton self-diffusion in Al-bearing bridgmanite calculated from *ab initio* MD trajectories using Eq. (2.1). D^{self} are similar to those calculated from MD simulations in Al-free bridgmanite (Peng and Deng (2024)). For example, the calculated D^{self} at 25 GPa and 2015 K is 7.7×10^{-9} $m^2\ s^{-1}$ for the $(Mg+2H)_{Si}$ substitution (Peng and Deng (2024)), and is slightly lower than the value reported here for Al-bearing bridgmanite at similar conditions ($D^{\text{self}} = 1.1\times 10^{-8}$ $m^2\ s^{-1}$ at 25 GPa and 2000 K). Our results are also consistent with those of other silicate minerals at similar pressures and temperatures. For example, the proton self-diffusion coefficient is 1.0×10^{-9} $m^2\ s^{-1}$ for Al-bearing bm at 1500 K and 25 GPa, which is about the same as the value reported for wadsleyite by Ohtani et al. (Ohtani and Zhao (2009)) ($D^{\text{self}} \sim 1\times 10^{-9}$ $m^2\ s^{-1}$ at around 25 GPa and 1400 K) and slightly higher than that reported by (Hae et al. (2006)). The calculated D^{self} at 2000 K and 25 GPa also falls within the range of D^{self} calculated for different water defect mechanisms in ringwoodite (Caracas and Panero (2017)), and is close to those extrapolated from an experimental single-crystal study (Sun et al. (2015)). A notable difference between proton diffusion in bm and MTZ compounds is that the activation energy is markedly smaller for proton diffusion in bm. Depending on the lithology, typical activation enthalpies for proton diffusion in ringwoodite and wadsleyite (Hernández et al. (2013)) are above 1.5 eV at 2500 K and 25 GPa (Caracas and Panero (2017)) whereas the activation enthalpy at the same PT condition for bm is only ∼ 0.4 eV.

A *decrease* in activation enthalpy with pressure from 25 to 75 GPa is surprising since we expect that the transition barrier height *increases* with increasing pressure because of greater lattice strain at the transition state at higher pressure. This can possibly be explained by a decrease in the difference in strain energy of the lattice between the equilibrium site and the transition state. If the strain energy at the equilibrium site increases more than the strain energy at the transition state with increasing pressure, the activation energy for diffusion is expected to decrease. A relatively high lattice strain at the equilibrium site promotes fast diffusion at high pressure and is likely to be intimately linked to a preferential partitioning of protons in ringwoodite and lower water solubility in bm compared to ringwoodite. Overall, we find that D^{self} is nearly constant $\sim 10^{-8}$ m^2 s^{-1} along the lower mantle average and hot geotherms, in good agreement with values reported for Al-free bridgmanite (Peng and Deng (2024)) (see Fig. 2). By contrast, D^{self} increases by nearly an order of magnitude from $\sim 10^{-10}$ m^2 s^{-1} to $\sim 10^{-9}$ m^2 s^{-1} along a cold slab geotherm down to about mid lower mantle depths.

3.2. Loss of water from the downgoing slabs

Our constraints on proton self-diffusion in bridgmanite allow us to calculate the flux of water using Eq. (2.2) from hydrated slab peridotite into dehydrated slab layers and the drier ambient lower mantle. We use Eq. (2.2) to calculate concentration profiles along cold, normal and hot mantle geotherms. The flux of water depends on the slab sinking rate, which is estimated to lie within the range of 9 to 25 mm/yr (van der Meer et al. (2018)) depending on depth-viscosity profiles. Correlations between tomographic images and plate tectonic reconstructions indicate an average slab speed of 12 ± 3 mm/yr (van der Meer et al. (2010, 2018)), which corresponds to about 100 Myr and 180 Myr before the slabs reach mid lower-mantle (1800 km) and lowermost mantle depths, respectively. Slab size and morphology also affect water loss, with slab-widths ranging from less than 500 km to more than 10 000 km and subducted slab edges typically extending 1000-1800 km deep and about 300 km thick as illustrated by the Mariana slab (edge ∼ 1400 km) or the New Hebrides slab (edge ∼ 1500 km) (van der Meer et al. (2018)). Slab size and morphology, however, change with depth due to variations in mantle viscosity and thermal conductivity. Slabs can possibly stretch and thin with decreasing viscosity or flatten, thicken, and contract with increasing viscosity (Rudolph et al. (2015)). They may combine with one another to form bigger clusters or detach into smaller fragments (Grima et al. (2020)). Highly viscous cold slab mantle, however, will probably not undergo extensive deformation and thinning and hence material length scales of material mixing are only ∼ meters at Gyr time-scales (Holzapfel et al. (2005); Manga (1996)). An inspection of tomographic images of the lower mantle (van der Meer et al. (2018)) suggests that slabs and slab remnants typically range from about $\mathrm{Vol}^{\mathrm{slab}}/\mathrm{Vol}^{\mathrm{mantle}} \sim 10^{-5}$ to $\sim 10^{-3}$ where $\mathrm{Vol}^{\mathrm{mantle}}$ is the volume of the entire mantle, and $\mathrm{Vol}^{\mathrm{slab}}$ is volume of the slab as interpreted from the tomographic images (van der Meer et al. (2018)). The hydrated core of the slab, however, will be smaller than this since the thermal diffusivity, κ, is at least an order of magnitude larger than D^{self} for protons (Fig. 2).

To take into account the slab surface topography, we calculate the outflux from hydrated slabs with various slab-surface-area to slab-volume ratios (i.e. SA:V) for a given slab volume ratio $\mathrm{Vol}^{\mathrm{slab}}/\mathrm{Vol}^{\mathrm{mantle}}$. The SA:V values chosen represent different typical slab morphologies as interpreted from the tomographic images (van der Meer et al. (2018)). Large lower mantle slabs represented by smooth “spheroid-like” or “cylindrical-like” bodies typically have SA:V values of ∼ 0.006 km^{-1}, whereas sheets of subducting slabs (Kiraly et al. (2020); van der Meer et al. (2018)) typically have slightly higher SA:V (∼ 0.009 km^{-1}). Surface topography details with lengths < 100 km are not captured by the spatial resolution of tomographic images, which is typically ∼ 100 km. Nevertheless, we also investigate water loss from hydrated slab cores with “rugged” surfaces, constructed by replacing a smooth interface with a wavy surface having amplitude and wavelengths similar to a proton’s average diffusion-lengthscale for a lower-mantle slab lifetime. Such “rugged” large-surface area slabs have a SA:V that is about 6 times larger than corresponding smooth objects.

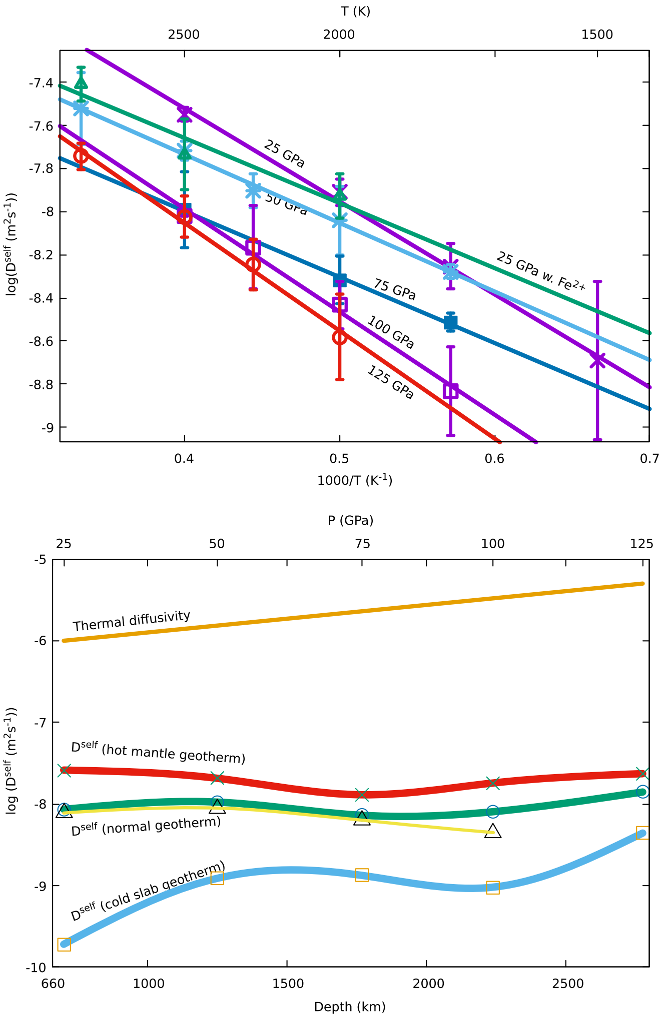

Fig. 2. Calculated proton self-diffusion coefficient in Al-bearing bm using *ab initio* MD and Eq. (2.1). Top figure shows Arrhenius plots for different pressures written as: $\mathrm{D}^{\mathrm{self}}/(\mathrm{m}^2\,\mathrm{s}^{-1}) = 3.0 \times 10^{-3}\exp(-0.37\ \mathrm{eV}/k_{\mathrm{B}}T)$ at 25 GPa, $D^{\mathrm{self}}/(\mathrm{m}^2\,\mathrm{s}^{-1}) = 1.6 \times 10^{-3}\exp(-0.27\ \mathrm{eV}/k_{\mathrm{B}}T)$ at 50 GPa, $D^{\mathrm{self}}/(\mathrm{m}^2\,\mathrm{s}^{-1}) = 1.1 \times 10^{-3}\exp(-0.26\ \mathrm{eV}/k_{\mathrm{B}}T)$ at 75 GPa, $D^{\mathrm{self}}/(\mathrm{m}^2\,\mathrm{s}^{-1}) = 2.3 \times 10^{-3}\exp(-0.41\ \mathrm{eV}/k_{\mathrm{B}}T)$ at 100 GPa, $D^{\mathrm{self}}/(\mathrm{m}^2\,\mathrm{s}^{-1}) = 2.3 \times 10^{-3}\exp(-0.43\ \mathrm{eV}/k_{\mathrm{B}}T)$ and $D^{\mathrm{self}}/(\mathrm{m}^2\,\mathrm{s}^{-1}) = 1.6 \times 10^{-3}\exp(-0.26\ \mathrm{eV}/k_{\mathrm{B}}T)$ at 25 GPa (w. Fe^{2+}). The error-bars are 2σ. Bottom figure shows D^{self} of protons in Al-bearing bm along an ambient mantle geotherm (green line) taken from Stixrude et al. (2009) but slightly adjusted to match a CMB temperature of 4000 K (Trønnes et al. (2019)). The cold (blue) and hot (red) slab geotherms are taken from (Nishi et al. (2014) and Trønnes et al. (2019)) respectively. The yellow line shows proton diffusion in Al-free bridgmanite (Peng and Deng (2024)). The thermal diffusivity is calculated from the thermal conductivity, k, taken from a diamond anvil cell (DAC) study (Edmund et al. (2024)) using $\kappa = k/\rho c_{\mathrm{p}}$. Here we use a specific heat, c_{p}, and density, ρ, of 449.9 J kg^{-1} K^{-1} and 5916.2 kg/m^3 respectively, taken from (Okuda et al. (2017)) for CMB conditions. The value of k is consistent with those found from experimental DAC data for bridgmanite and post-perovskite in lower mantle lithologies (Okuda et al. (2017, 2020); Ohta et al. (2012)) as well as those from thermodynamic modeling (Manthilake et al. (2011)).

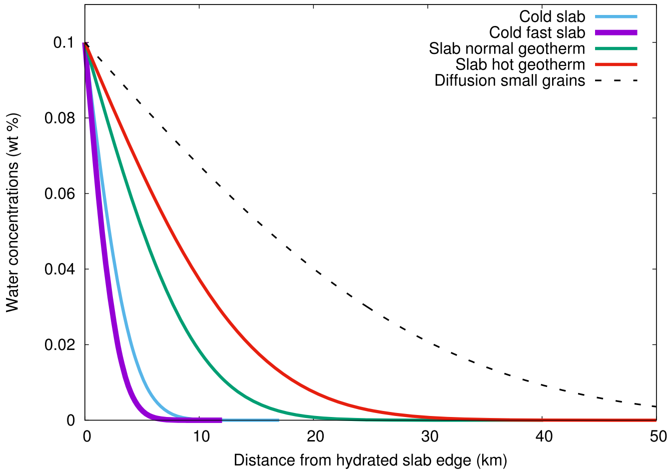

Fig. 3. Concentration profiles as a function of the distance x perpendicular to the hydrated slab-ambient-mantle interface for cold (blue curves), normal (green curve) and hot (red curve) mantle temperatures at mid lower-mantle depths (1800 km) calculated using Eq. (2.2). For fast (thick line) and normal (thin lines) slabs we assume that it takes 50 and 100 Myr before the slab reaches mid lower-mantle depths after entering the lower mantle. This is consistent with fast- and average slab-sinking rates of 20 and 12 mm/yr respectively (van der Meer et al. (2018)). The profiles are drawn assuming a constant water concentration of 0.1 wt% within the hydrated portion of the slab and that the surrounding material is dry. The slabs have a SA:V $= 9 \times 10^{-3}$ km^{-1} and proton diffusion coefficients are average lower mantle values: i.e. $D^{\text{self}} = 1.6 \times 10^{-9}$ m^2 s^{-1}, 9.0×10^{-9} m^2 s^{-1} and 2.0×10^{-8} m^2 s^{-1} for cold, ambient/average and hot mantle temperatures respectively. The black dashed line shows a profile representative of proton diffusivity in polycrystalline bm with very small grains ∼ 10 micrometer). The red line also represents a profile for primordial-like water-rich heterogeneities - entrained from the lowermost-mantle structures (i.e. LLSVPs) by deep-rooted mantle plumes - rising rapidly (with speed 25 mm/yr) through the lower mantle.

Fig. 3 shows examples of water concentrations at a distance x from the edge of the wet part of the slab into the dry-slab and ambient mantle at mid-mantle depths (∼ 1800 km) for a vertically sinking slab at different temperatures and slab speeds. The profiles for average ambient mantle temperature (green) and cold slab temperatures (blue) - representative for sinking slabs at the top of the lower mantle to mid-mantle depths - show that loss of water from slabs due to proton lattice diffusion only rehydrates the upper part of the lower mantle *locally* (i.e. on length-scale of a few km) near the hydrated part of the slab along the slab paths. We can estimate the proton traveling lengths, d_w, as a function of time, t, away from the hydrated slab core (interdiffusion) using $d_w = \sqrt{D^{\text{self}} t}$ for representative average values of proton diffusivity. The resulting profiles are plotted for different mantle geotherms in Fig. 4 together with an estimated average (lower mantle) thermal diffusivity profile (Edmund et al. (2024)).

Lattice diffusion length scales of protons in bm away from the wet-dry interface during the slab's journey to the lowermost mantle (∼ 200 Myr), are less than 3 km for a representative cold lower mantle geotherm and ∼ 5 km for an ambient lower mantle geotherm. During the last 3-5 billion years, d_w is only a few tens of km, emphasizing that recycled water is far from homogeneously distributed in the lower mantle, but rather controlled by the trajectories of subducted slabs and its distribution within them. Grain boundary diffusion, however, could possibly alter these estimates since protons in general diffuse much faster along grains than within lattices. If the grains are very small (i.e. on the size of 10 micron or less), grain-boundary diffusion may significantly enhance the overall bulk diffusivity (also at high temperatures). Bulk diffusivities for olivine, wadsleyte and ringwoodite aggregates with very small grain sizes (∼ 10 μm) are typically about one order of magnitude higher than those for single crystals (Demouchy (2010); Huang et al. (2005); Ohtani and Zhao (2009); Sun et al. (2015); Caracas and Panero (2017); Yoshino et al. (2008)). Therefore, it is reasonable to assume that the proton diffusion coefficient for polycrystalline bridgmanite with very small grain sizes (∼ 10 μm) is also about one order of magnitude higher than that in the crystalline phase, and we can therefore estimate proton traveling lengths for polycrystalline bridgmanite with tiny grains. The calculated d_w for cold slabs with such small grains (∼ 10 μm) at mid-mantle depths are less than 20 km and about 25-30 km when slabs reach the lowermost mantle. Predictions of lower mantle grain sizes, however, range from a few tens of micrometers to centimeter (Fei et al. (2021); Solomatov et al. (2002)) suggesting that the bulk diffusion coefficient in the lower mantle is likely to be markedly smaller than that of polycrystalline bm when the grains are ∼ 10 μm. The calculated d_w in polycrystalline bm with such small grains therefore probably provides upper bound constraints on proton interdiffusion length-scales in the lower mantle.

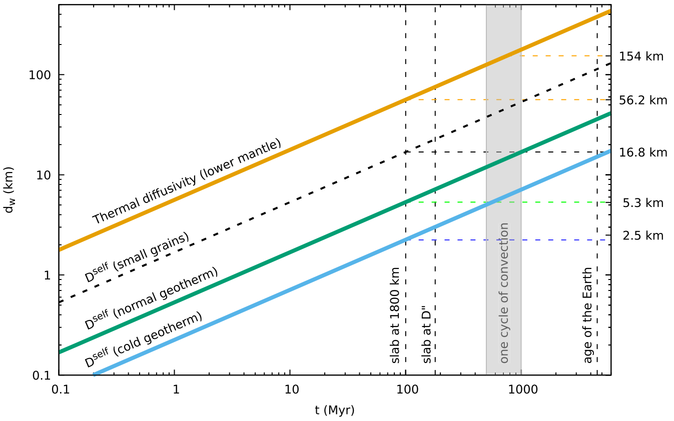

Fig. 4. Average diffusion length scales for protons in bm along cold and normal geotherms, together with estimated diffusion lengths in polycrystalline bm with very small grain sizes (< 10 μm), from $d_w = \sqrt{D^{\text{self}} t}$. The thermal diffusivity, self diffusion coefficients and estimated diffusion in polycrystalline bm are the same as those used to plot Fig. 3 (see Fig. 3 caption for values used).

In Fig. 5 and Table 1 (supplemental information) we report net loss of water from downgoing slabs to dry slab peridotite/ambient mantle for different slab speeds, geotherms and SA:V. In general, we find that slabs lose very little water and the outflow of water is less sensitive to slab topography and slab speed than it is to slab temperature (i.e. proton diffusivity). A typical slab with an average speed of 12 mm/yr and SA:V $= 0.009$ km^{-1} is expected to lose far less than 1% of its total water content on its journey through the lower mantle to the CMB. An upper bound constraint on water loss for slow slabs with high values of SA:V is about 1% of the total water content of the slab.

3.3. Lower mantle water distribution

Because the fate of recycled water in the lowermost mantle is so closely tied to that of the slab material that hosts it, it is important to consider possible slab trajectories in the lower mantle (Fig. 6) to map the water distribution. Generally, when the slab material has reached the lowermost mantle, it is thought to be swept by large-scale (viscous) mantle flow toward the two Large Low Shear Velocity Provinces (LLSVPs) (Torsvik et al. (2016)). Broad-scale upwellings above the LLSVPs (Conrad et al. (2013)) may capture this slab material and bring it back toward the upper mantle. For typical rates of lower mantle flow (∼10-20 mm/yr), this journey of ∼ 10 000 km would require a transit time as long as 0.5-1.0 Gyr. Our estimates of water loss from the slab remnants show that the slabs lose less than 1% of their total water content on their journey back to the MTZ (see Table 1 in SI). After returning to the MTZ, this transported water may be temporarily stored in the transition zone and eventually outgass at hotspots or the mid-ocean ridge system (completing a solid-earth water cycle).

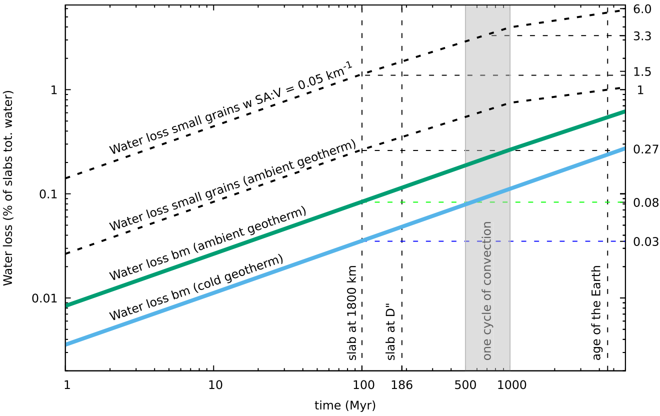

Fig. 5. Net water loss from lower mantle slabs/slab remnants to the ambient mantle as a function of lower mantle residence time. The slabs have the same SA:V as typical sheets of slab lithosphere with width and thickness of 1200 km and 300 km (i.e. SA:V = $0.009\ \mathrm{km}^{-1}$) as well as an example of water loss of slabs with more "rugged" surfaces (i.e. with SA:V = $0.05\ \mathrm{km}^{-1}$) constructed as explained in the main text. Loss of water from slabs containing bm with grains less than 10 μm are also displayed. The proton self diffusion coefficients are the same as those reported in Fig. 3.

Given that water remains within slab material in the mantle, we can use global fluxes to estimate water transport rates within the solid earth water cycle. Since the Mesozoic, slabs have removed an average of about 4 km^2 of oceanic lithosphere per year (Crameri et al. (2019)). If we assume an average thickness of the oceanic lithosphere of 80 km, this implies a slab flux rate of 1.1×10^{21} kg/Myr, which would fill the lower mantle in about 3 Gyr. This implies that the plate tectonic system has processed a mass equal the lower mantle about once during the age of the Earth. One ocean mass (1 OM = 1.4×10^{21} kg) of water can be subducted by this system in 3 Gyr if slabs transport an average of 0.044 wt% water into the lower mantle. Since, however, the warmer edges of the cold slabs are likely to be dehydrated before entering the lower mantle (van Keken et al. (2011)), only the cold inner core of subducted slabs, up to about 35 km thick for the coldest slabs, will maintain an elevated concentration of water. For example, cold slab cores that are 35 km thick and hydrated at 0.1 wt% would also bring one OM of water into the lower mantle in about 3 Gyr. At this rate, slabs in the lower mantle, which subducted during the past 500-1000 Myr (one lower mantle transit time), may currently store up to 0.3 OM of water.

The outer, dehydrated, portion of the slab, probably less than a few tens of km wide, would become slowly rehydrated as it passes through the lower mantle by proton diffusion from the hydrated portion of the slab. The calculated d_w for protons is approximately 12-17 km for $D^{\mathrm{self}} = 9.0 \times 10^{-9}\ \mathrm{m}^2\mathrm{s}^{-1}$ and a transport time $t \sim$ 500-1000 Myr before ascent. If proton diffusion along grain boundaries dominates with $\mathrm{D}^{\mathrm{self}} = 9.0 \times 10^{-8}\ \mathrm{m}^2\mathrm{s}^{-1}$, then the proton average traveling length increases to $d_w \sim 40 - 50$ km. By contrast, thermal diffusivity is of order $10^{-6}\ \mathrm{m}^2\mathrm{s}^{-1}$ (Edmund et al. (2024)), which gives a lengthscale of $d_s \sim$ 125-180 km. Thus, cold thermal anomalies associated with subducted slabs spread much faster than the water carried by the slabs. The higher strength associated with these cold temperatures may help to protect the slab's hydrated core, allowing slabs to travel with their water along with larger-scale mantle flow (Fig. 6).

Water in slab material that gets subducted into the lower mantle is unlikely to be significantly sampled by plumes, for two reasons. First, plumes rise from the hot lower thermal boundary layer that sits on the core-mantle boundary (Duncan and Richards (1991); Cagney et al. (2016)). This boundary layer may be pushed by large-scale mantle flow toward the LLSVP edges, from which plumes rise toward the surface (Heyn et al. (2020)). Subducted water stored in the original cores of slabs, either in wet bridgmanite or hydrated silica from entrained crustal minerals, can diffuse at most only a few tens of km as the slabs transit the mantle (Fig. 4). Because the cold temperatures of the slab diffuse outward more quickly, water can become trapped within the cold slab interior (Fig. 6). This cold slab region should be stiffer than its surroundings, and thus the water it holds is not likely to interact with the thermal boundary layer on the core-mantle boundary, and is therefore unlikely to be drawn into plumes. Instead, water carried upward by plumes likely samples water from the core-mantle boundary region (see the next section) (Hallis et al. (2015)) or possibly from storage reservoirs in the LLSVPs. Indeed, the LLSVPs may be partly composed of recycled oceanic crust (Trønnes et al. (2019)), containing possibly hydrated silica (Walter (2021)), which can become entrained in the hot center of the plume conduits (Jones et al. (2016)).

Second, the plume flux is smaller than the subduction flux, which indicates that downward subduction is largely replaced by mantle return flow, rather than plumes. Specifically, we estimate the total plume mass flux as 2.3×10^{20} kg/Myr, which is about one quarter of the subduction flux rate estimated above. This rate is based on the global plume buoyancy flux of 46.2 Mg/s (Hoggard et al. (2020)) and the assumption that thermal buoyancy only accounts for $\alpha\Delta T = (3\times10^{-5}\mathrm{K}^{-1})(225\,^{\circ}\mathrm{C}) = 1/148$ of the plume's total mass flux. Some periods in the past (e.g., the Cretaceous) may have experienced significantly more plume activity than this estimate suggests. Nevertheless, only a fraction of the lower mantle mass of 3×10^{24} kg could be fully processed by plumes in the past 3 Gyr. Thus, most subducted water is transported by background mantle flow, instead of plumes.

Since it takes 500-1000 Myr for subducted material to descend into the lower mantle and re-emerge into the transition zone, water that was subducted in the Phanerozoic and earlier may still reside within cold slab material in the lower mantle. Applying the current regassing rates of $2\times10^{11} - 4\times10^{11}$ kg/yr (van Keken et al. (2011); Parai and Mukhopadhyay (2012)) to the past 500-1000 Myr suggests that 0.07 to 0.28 OM of recycled water may currently be stored in the lower mantle. This estimate of water storage implies that the average hydrated slab core would be 20-30 km thick and hydrated at 0.1 wt%. Such estimates are consistent with estimates of slab core thickness (van Keken et al. (2011)) and below the water storage capacity of bridgmanite in peridotite (Litasov et al. (2003); Fu et al. (2019); Murakami et al. (2002)). We note that even faster regassing rates may have applied earlier in the Phanerozoic because faster subduction at past times could bring even more water into Earth's deep interior. For example, regassing rates were approximately double today's rate throughout the Cretaceous, and at times up to 4 times faster (Karlsen et al. (2019)). If we allow that regassing rates in the Phanerozoic and earlier may have been double that of today, the lower mantle could currently store 0.5 OM of recycled water within subducted slab material. On the other hand, the water storage in the lower mantle may be reduced if only part of the water that is subducted beyond the back-arc successfully makes it to the MTZ and into the lower mantle (Walter (2021)). Regardless of these uncertainties, lower mantle slabs likely provide temporary storage for water as it transits back to the TZ. The retention of water within the slabs, coupled with the long residence time of slabs in the lower mantle, means that transiting slab remnants carry significant quantities of recycled water.

3.4. Origin of low D/H values sampled by deep-rooted plumes and core-mantle water exchange processes

Although a large fraction of water is likely to remain within the slab remnants and will eventually return to the transition zone, water in slab material that approaches the core-mantle boundary can also possibly react with, or partition into, the core if the core remains undersaturated in hydrogen/water (Li et al. (2022b)). We can roughly constrain the possible influx of water from slab remnants into the core over the last 3 Gyr from Eq. (2.2) using representative values of proton diffusivity in the outermost core and assuming a largely stagnant outermost E" layer. Using a proton self-diffusion coefficient of $8 \times 10^{-8}\ \mathrm{m}^2\,\mathrm{s}^{-1}$ in a liquid iron alloy at 4500 K (Li et al. (2022a)) and assuming that the slab remnants

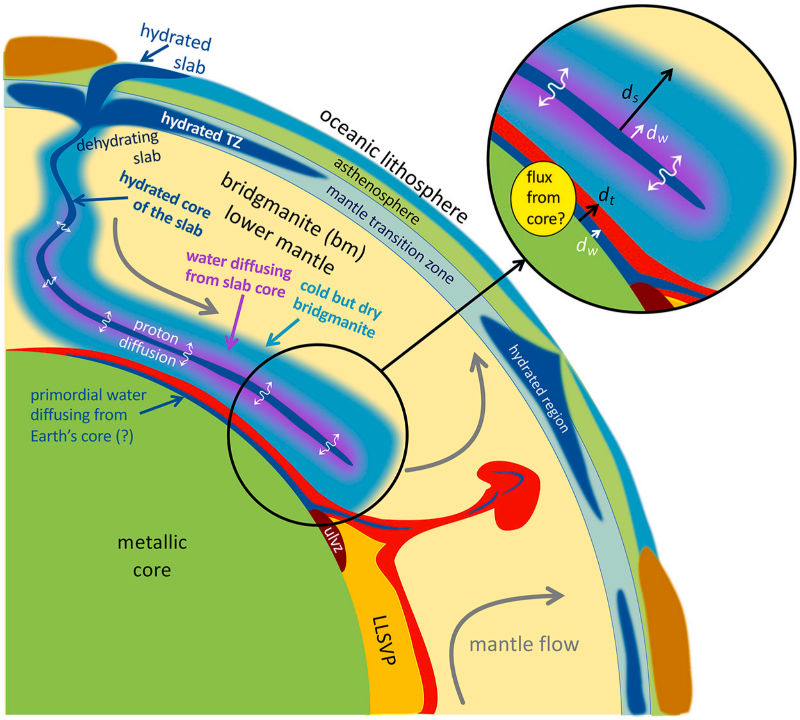

Fig. 6. Possible trajectory of subducted water within the lower mantle. Water that is retained within the slab after it passes through the transition zone will be stored within the cold hydrated core of the slab (dark blue). We have shown that d_w, which is the length scale for proton diffusion away from this hydrated core, is much smaller than d_s, which is the length scale for thermal diffusion away from slab (see inset). This suggests that water will remain within the cold interior of the slab, and isolated from both the ambient mantle and the core-mantle boundary region, as it transits the lower mantle toward the LLSVP regions and eventually returns toward the partially-hydrated transition zone. Because the ambient mantle remains dry, water may diffuse from the metallic core into a region of thickness d_w (dark blue region above the CMB). This primordial water will remain within the lower thermal boundary layer, which has a larger thickness d_t because diffusion of heat is faster than diffusion of water (see inset). Plumes rising from CMB region may thus bring primordial water toward the surface.

are water saturated (with ~ 0.1 wt% water) near the CMB, we find that less than 10% of the recycled water in the slab material is lost to the core since subduction was initiated. This estimate probably represents a significant overestimate since we argue above that the hydrated parts of the old slabs are unable to approach the CMB because they are surrounded by stiff zones of cold and dehydrated mantle peridotite (Fig. 6). If the bottom layer of the lowermost mantle (a few tens km thick) is essentially dry, water could rather be drawn *out of* the core as we discuss below. Overall, far less than 0.1 OM of recycled water, if any, has entered the core over the last 3 Gyr due to diffusional influx.

The diffusivity of protons in bridgmanite can also provide constraints on the extent of possible primordial water reservoirs in the lower mantle. Melt inclusions in OIBs from, e.g. Baffin Island, often have anomalously low D/H and high He^3/He^4 values suggesting that these inclusions are sampling primordial water that may have become trapped and preserved in the core or somewhere deep in the lower mantle despite 4 Gyr of mantle convection (Stixrude and Karki (2005); Labrosse et al. (2007); Caracas et al. (2019)). Fig. 4 shows that d_w is a few tens of km after about 4 Gyr, placing constraints on the size of possible primordial reservoirs/heterogeneities isolated from convection if they are to exist over the age of the Earth. The convective and partly molten ULVZs will probably not be able to hold primordial water alone over such a long time, but can act as a "staging post" for primordial water leakage from, e.g., the core to feed plume conduits. Mantle plumes can also sample from both the LLSVPs and the lower thermal boundary layer of the core-mantle boundary region (Heyn et al. (2020); Cagney et al. (2016); Duncan and Richards (1991)). The Earth's metallic core and the LLSVPs therefore provide potential sources for long-term storage of primordial water.

In spite of the highly sidrophile nature of protons, slow direct outgassing of primordial water from the core to the lowermost mantle is still possible, at least locally, driven by an "out of equilibrium" water-undersaturated (dry) lowermost mantle. Even in lowermost mantle regions where cold wet slabs were deposited, the bottom few tens of km above the CMB may still be very dry since the length scales of proton outgassing from slab remnants are too short even at Gyr time scale to wetten the bottom of the D" (Peng and Deng (2024)). Water from the hydrated part of the slabs may therefore be unable to reach the CMB. A very dry region near the CMB could drive (slow) outgassing of primordial water from the core. Plumes rising from the lower boundary layer can then entrain this outgassed primordial water, uncontaminated by recycled water, and bring it toward the Earth's surface (Fig. 6). Since $d_w \sim 10$ km for protons (along a representative hot thermal mantle profile) is much shorter than typical plume dimensions of $\sim$ 100-300 km (French and Romanowicz (2015)), there will be little (diffusional) water exchange ($< 1\%$) between plumes and the ambient mantle in the $\sim$ 50 Myr ascent time of plume-entrained material. That is primitive D/H ratios observed within erupted plume material likely reflect the ratios within the deepest mantle *unless* D and H are diffusionally fractionated. We can estimate the extent of diffusional fractionation of the two isotopes within a plume heterogeneity of bridgmanitic material during the $\sim$ 50 Myr ascent through the lower mantle by comparing the proton and deuterum self diffusion coefficients in bm. From our calculated $D^{\text{self proton}}$, $D^{\text{self deuterium}}$ can be obtained from the square root of their mass ratio using (Claire (1966); Van Orman and Krawczynski (2015)): $D^{\text{self deuterium}} = D^{\text{self proton}} \times (\sqrt{\frac{m_D}{m_H}} - 1) = 0.4 \times D^{\text{self proton}}$. The interdiffusion length-scale of deuterium is therefore $0.6 \times d_w$, which indicates that deuterium and proton could be diffusionally fractionated in primordial-like heterogeneities if they are stretched to thin filaments smaller than typical proton traveling lengths in $\sim$ 50 Myr. Heterogeneities that remain larger than this (e.g. a blob with $r > 10$ km) will be able to preserve the D/H ratio in their cores during ascent to the MTZ (Farnetani et al. (2018)).

Estimating the volume of primordial water in the deep Earth, and the rate of water leakage toward the surface via plumes, is challenging because core-mantle water fluxes are strongly dependent on the water distribution in the young Earth, which itself is poorly constrained. As discussed above, if the MO was largely depleted in water before it froze, the lowermost mantle could have been essentially dry for a long time, favoring the flow of water *out of* the core despite of the siderophile nature of protons (Li et al. (2022b)). Such a scenario is probably dependent on the MO redox state. That is, under highly reducing (enstatite-like) conditions, the magma ocean probably produced H_2 (and CO) rich gases (Schaefer and Fegley (2010)) that can readily outgas, escape the Earth (Bower et al. (2022); Walter (2021)), and deplete the silicate melt/mantle. On the other hand, more oxidizing conditions, which could be present if accreted materials were made largely from CI and CM carbonaceous chondrites (Schaefer and Fegley (2010)), should lead to high solubility of water in the MO and hydrogen dissolution in growing crystals. These processes would hinder - or slow down - extensive early outgassing. This suggests, in turn, that bridgmanite/post-perovskite could have stored a substantial amount of primordial water during the 4 Gyr since the freezing of the MO, in addition to the recycled water that is currently stored within the mantle minerals of transiting cold slabs and accumulations of oceanic crustal material. Water trapped in the lowermost mantle could potentially diffuse into the outer core (Ohtani and Zhao (2009); Kim et al. (2023)) under these conditions.

The water distribution of the lowermost mantle is highly heterogeneous and under constant change. Protons can travel both into and out of the core depending on short and intermediate length-scales of the water distribution in the lowermost mantle. However, even in cases where the lowermost mantle contains a substantial amount of water, over Gyr length scales, the relatively "slow" diffusion of protons in bm suggests that there has been little exchange of water/protons between the core and the mantle compared to the total hydrogen amount. The current core content thus largely reflects the initial delivery of water from mainly chondritic material with possible addition from nebular ingassing (Wu et al. (2018); Li et al. (2022b)).

4. Conclusions

Ab initio molecular dynamics simulations offer a powerful atomistic insight into proton diffusion mechanisms in lower mantle minerals and can help to constrain flux rates across boundaries to map deep water cycles occurring throughout Earth's history. From these atomistic trajectories we extract the proton self diffusion coefficient for Al-bearing bridgmanite at lower mantle conditions and fit Arrhenius equations as follows: $\mathrm{D}^{\mathrm{self}}/(\mathrm{m}^2\,\mathrm{s}^{-1}) = 3.0 \times 10^{-3} \exp(-0.37\ \mathrm{eV}/k_{\mathrm{B}}T)$ at 25 GPa, $D^{\mathrm{self}}/(\mathrm{m}^2\,\mathrm{s}^{-1}) = 1.6 \times 10^{-3} \exp(-0.27\ \mathrm{eV}/k_{\mathrm{B}}T)$ at 50 GPa, $D^{\mathrm{self}}/(\mathrm{m}^2\,\mathrm{s}^{-1}) = 1.1 \times 10^{-3} \exp(-0.26\ \mathrm{eV}/k_{\mathrm{B}}T)$ at 75 GPa, $D^{\mathrm{self}}/(\mathrm{m}^2\,\mathrm{s}^{-1}) = 2.3 \times 10^{-3} \exp(-0.41\ \mathrm{eV}/k_{\mathrm{B}}T)$ at 100 GPa, $D^{\mathrm{self}}/(\mathrm{m}^2\,\mathrm{s}^{-1}) = 2.3 \times 10^{-3} \exp(-0.43\ \mathrm{eV}/k_{\mathrm{B}}T)$ and $D^{\mathrm{self}}/(\mathrm{m}^2\,\mathrm{s}^{-1}) = 1.6 \times 10^{-3} \exp(-0.26\ \mathrm{eV}/k_{\mathrm{B}}T)$ at 25 GPa (w. Fe^{2+}). These rates imply a proton diffusion length-scale less than 10 km in lower mantle peridotite during the 150-200 million years timescale for slab material to sink through the lower mantle. Even at the age of the Earth the proton diffusion traveling length is small compared to the sizes of the slab remnants. Therefore only the outer part of a wet slab interior will become partly degassed, while the water concentration in the slab's inner core will remain constant. Only a small fraction of the water that manages to escape the wet slab core will be released into the surrounding ambient mantle.

Assuming that a lower mantle overturn takes 500-1000 Myr and using present-day ingassing rates of $2-4 \times 10^{11}$ kg/yr (van Keken et al. (2011); Parai and Mukhopadhyay (2012)) suggests that 0.1-0.3 OM of water remains trapped within slabs that are transiting the lower mantle. This water may be stored within cold cores of lower mantle slabs that are 20-35 km thick and remain hydrated at levels of 0.10 wt% as they transit the lower mantle (Fig. 6). Protected by the cold, stiff, and dehydrated exterior of the slab (Fig. 6), this water within the slab interior is unlikely to come into sufficiently close contact with the metallic core to be drawn further downwards, despite water's strong affinity to iron. This suggests that recycled water may not react with iron to form hydroxides, and indicates little influx of recycled water into the core over the age of the Earth. By contrast, deep-rooted mantle plumes may entrain materials containing primordial-like water with anomalously low deuterium/hydrogen ratio that has diffused from unprocessed reservoirs in the lowermost mantle and/or the core into the lowermost (dry) mantle. Because of "slow" proton diffusion, plumes may preserve these signals in entrained heterogeneities (e.g. a blob with $r > 10$ km) as they rise toward the surface.

5. Supplementary materials

Table 1

Net water loss from slabs (remnants) in the lower mantle, calculated from the time they enter the lower mantle until 1) they reach mid lower mantle depths (1800 km) and 2) complete a lower mantle cycle. We analyze water loss from slabs along different geotherms (temperatures), with different slab residence times (slab speeds) and SA:V ratios. Three different slab morphologies are investigated including those represented by smooth compact "sphereoid-like" slabs with SA:V = 0.006 km^{-1}, lower mantle slabs with the same shape and SA:V as typical sheets of slab lithosphere with width 1200 km and thickness 300 km (SA:V = 0.009 km^{-1}), as well as slabs with "rugged" surfaces or stretched filaments with SA:V = 0.05 km^{-1} constructed as explained in the main text. Calculations marked as "^{a}" are estimated water loss from slabs with polycrystalline bm containing grains that are less than ~ 10 μm.

geotherm	D^{self} (10^{-9} m^2/s)	Slab speed (mm/year)	SA:V (km^{-1})	Water loss (1800 km) (% slab water cont.)	Water loss (LM cycle) (% slab water cont.)
cold	1.6	9	0.0060	0.025	0.074
	1.6	9	0.0091	0.039	0.112
	1.6	9	0.0481	0.205	0.593
normal	9.0	9	0.0060	0.061	0.176
	9.0	9	0.0091	0.092	0.265
	9.0	9	0.0481	0.487	1.407
normal	9.0	12	0.0060	0.055	0.157
	9.0	12	0.0091	0.084	0.237
	9.0	12	0.0481	0.444	1.258
hot	9.0	20	0.0060	0.039	0.124
	9.0	20	0.0091	0.059	0.187
	9.0	20	0.0481	0.315	0.995
hot	20	20	0.0060	0.059	0.185
	20	20	0.0091	0.088	0.279
	20	20	0.0481	0.470	1.482
normal^a	90	12	0.0060	0.176	0.458
	90	12	0.0091	0.265	0.692
	90	12	0.0481	1.401	3.674

CRediT authorship contribution statement

Chris E. Mohn: Writing – review & editing, Writing – original draft, Validation, Resources, Project administration, Methodology, Investigation, Funding acquisition, Formal analysis, Data curation, Conceptualization. **Razvan Caracas:** Writing – review & editing, Writing – original draft, Visualization, Validation, Resources, Methodology, Investigation, Funding acquisition, Conceptualization. **Clinton P. Conrad:** Writing – review & editing, Writing – original draft, Visualization, Validation, Resources, Methodology, Investigation, Formal analysis, Conceptualization.

Declaration of competing interest

The authors declare that they have no conflict of interest.

Acknowledgements

This research was partly supported by the Research Council of Norway (NFR), project numbers 332523 (PHAB), 223272 (CEED), 325567 (HIDDEN), and 288449 (MAGPIE). The simulations were performed on resources provided by Sigma2 - the National Infrastructure for High-Performance Computing and Data Storage in Norway (Uninet2 Sigma2, NN2916K, and NN9697K grants). The authors would like to thank Reidar Trønnes for fruitful discussions.

Data availability

Data will be made available on request.

References

Ammann, M.W., Brodholt, J.P., Wookey, J., Dobson, D.P., 2010. First-principles constraints on diffusion in lower-mantle minerals and a weak D” layer. Nature 465, 462–465. https://doi.org/10.1038/nature09052.

Bower, D.J., Hakim, K., Sossi, P.A., Sanan, P., 2022. Retention of water in terrestrial magma oceans and carbon-rich early atmospheres. Planet. Sci. J. 3, 93. https://doi.org/10.3847/PSJ/ac5fb1.

Cagney, N., Crameri, F., Newsome, W., Lithgow-Bertelloni, C., Cotel, A., Hart, S., Whitehead, J., 2016. Constraining the source of mantle plumes. Earth Planet. Sci. Lett. 435, 55–63. https://doi.org/10.1016/j.epsl.2015.12.008.

Caracas, R., Hirose, K., Nomura, R., Ballmer, M.D., 2019. Melt–crystal density crossover in a deep magma ocean. Earth Planet. Sci. Lett. 516, 202–211. https://doi.org/10.1016/j.epsl.2019.03.031.

Caracas, R., Panero, W.R., 2017. Hydrogen mobility in transition zone silicates. Prog. Earth Planet. Sci. 4, 9. https://doi.org/10.1186/s40645-017-0119-8.

Claire, A.D.L., 1966. Some comments on the mass effect in diffusion. Philos. Mag. J. Theor. Exp. Appl. Phys. 14, 1271–1284. https://doi.org/10.1080/14786436608224292.

Conrad, C.P., Steinberger, B., Torsvik, T.H., 2013. Stability of active mantle upwelling revealed by net characteristics of plate tectonics. Nature 498, 479–482. https://doi.org/10.1038/nature12203.

Crameri, F., Conrad, C.P., Montési, L.R., Lithgow-Bertelloni, C., 2019. The dynamic life of an oceanic plate. Tectonophysics 760, 107–135. https://doi.org/10.1016/j.tecto.2018.03.016.

Crowley, J.W., Gérault, M., O’Connell, R.J., 2011. On the relative influence of heat and water transport on planetary dynamics. Earth Planet. Sci. Lett. 310, 380–388. https://doi.org/10.1016/j.epsl.2011.08.035.

Demouchy, S., 2010. Diffusion of hydrogen in olivine grain boundaries and implications for the survival of water-rich zones in the Earth’s mantle. Earth Planet. Sci. Lett. 295, 305–313. https://doi.org/10.1016/j.epsl.2010.04.019.

Duncan, R.A., Richards, M.A., 1991. Hotspots, mantle plumes, flood basalts, and true polar wander. Rev. Geophys. 29 (1), 31–50. https://doi.org/10.1029/90RG02372.

Edmund, E., Chuvashova, I., Konôpková, Z., Husband, R., Strohm, C., Appel, K., Bähtz, C., Ball, O., Bouffetier, V., Brugman, K., Buakor, K., Chantel, J., Chariton, S., Duff, M., Dwivedi, A., Glazyrin, K., Hosseini-Saber, S.M.A., Jaisle, N., Laurus, T., Li, X., Masani, B., McHardy, J., McMahon, M., Merkel, S., Mohrbach, K., Mondal, A., Morard, G., Prakapenka, V.B., Prescher, C., Ryu, Y.J., Schwinkendorf, J.P., Tang, M., Younes, Z., Sanchez-Valle, C., Liermann, H.P., Badro, J., Lin, J.F., McWilliams, R.S., Goncharo, A.F., 2024. The thermal conductivity of bridgmanite at lower mantle conditions using a multi-technique approach. J. Geophys. Res., Solid Earth 129, e2024JB028823. https://doi.org/10.1029/2024JB028823.

Farnetani, C.G., Hofmann, A.W., Duvernay, T., Limare, A., 2018. Dynamics of rheological heterogeneities in mantle plumes. Earth Planet. Sci. Lett. 499, 74–82. https://doi.org/10.1016/j.epsl.2018.07.022.

Fei, H., Faul, U., Katsura, T., 2021. The grain growth kinetics of bridgmanite at the topmost lower mantle. Earth Planet. Sci. Lett. 561, 116820. https://doi.org/10.1016/j.epsl.2021.116820.

French, S., Romanowicz, B., 2015. Broad plumes rooted at the base of the Earth’s mantle beneath major hotspots. Nature 525, 95–99. https://doi.org/10.1038/nature14876.

Frost, D.J., Liebske, C., Langenhorst, F., McCammon, C.A., Trønnes, R.G., Rubie, D.C., 2004. Experimental evidence for the existence of iron-rich metal in the Earth’s lower mantle. Nature 428, 409–412. https://doi.org/10.1038/nature02413.

Fu, S., Yang, J., Karato, S.i., Vasiliev, A., Presniakov, M.Y., Gavriliuk, A.G., Ivanova, A.G., Hauri, E.H., Okuchi, T., Purevjav, N., Lin, J.F., 2019. Water concentration in single-crystal (Al, Fe)-bearing bridgmanite grown from the hydrous melt: implications for dehydration melting at the topmost lower mantle. Geophys. Res. Lett. 46, 10346–10357. https://doi.org/10.1029/2019GL084630.

Grima, A.G., Lithgow-Bertelloni, C., Crameri, F., 2020. Orphaning regimes: the missing link between flattened and penetrating slab morphologies. Front. Earth Sci. 8, 374. https://doi.org/10.3389/feart.2020.00374.

Hae, R., Ohtani, E., Kubo, T., Koyamaa, T., Utada, H., 2006. Hydrogen diffusivity in wadsleyite and water distribution in the mantle transition zone. Earth Planet. Sci. Lett. 243, 141–148. https://doi.org/10.1016/j.epsl.2005.12.035.

Hallis, L.J., Huss, G.R., Nagashima, K., Taylor, G.J., Halldórsson, S.A., Hilton, D.R., Mottl, M.J., Meech, K.J., 2015. Evidence for primordial water in Earth’s deep mantle. Science 350, 795–797. https://doi.org/10.1126/science.aac4834.

Hernández, E.R., Alfé, D., Brodholt, J.P., 2013. The incorporation of water into lower-mantle perovskites: a first-principles computational study. Earth Planet. Sci. Lett. 364, 37–43. https://doi.org/10.1016/j.epsl.2013.01.005.

Heyn, B.H., Conrad, C.P., Trønnes, R.G., 2020. How thermochemical piles can (periodically) generate plumes at their edges. J. Geophys. Res., Solid Earth 125, e2019JB018726. https://doi.org/10.1029/2019JB018726.

Hoggard, M.J., Parnell-Turner, R., White, N., 2020. Hotspots and mantle plumes revisited: towards reconciling the mantle heat transfer discrepancy. Earth Planet. Sci. Lett. 542, 116317. https://doi.org/10.1016/j.epsl.2020.116317.

Holzapfel, C., Rubie, D.C., Frost, D.J., Langenhorst, F., 2005. Fe-Mg interdiffusion in $(Mg, Fe)SiO_3$ perovskite and lower mantle reequilibration. Science 309, 1707–1710. https://doi.org/10.1126/science.1111895.

Houser, C., 2016. Global seismic data reveal little water in the mantle transition zone. Earth Planet. Sci. Lett. 448, 94–101. https://doi.org/10.1016/j.epsl.2016.04.018.

Hsu, H., Yu, Y.G., Wentzcovitch, R.M., 2012. Spin crossover of iron in aluminous $MgSiO_3$ perovskite and post-perovskite. Earth Planet. Sci. Lett. 359–360, 34–39. https://doi.org/10.1016/j.epsl.2012.09.029.

Huang, X., Xu, Y., Karato, S. ichiro, 2005. Water content in the transition zone from electrical conductivity of wadsleyite and ringwoodite. Nature 434, 746–749. https://doi.org/10.1038/nature03426.

Humphrey, W., Dalke, A., Schulten, K., 1996. VMD – visual molecular dynamics. J. Mol. Graph. 14, 33–38. https://doi.org/10.1016/0263-7855(96)00018-5.

Jacucci, G., Rahman, A., 1978. Diffusion of F^- ions in CaF_2. J. Chem. Phys. 69, 4117. https://doi.org/10.1063/1.437091.

Jones, T., Davies, D., Campbell, I., Wilson, C., Kramer, S., 2016. Do mantle plumes preserve the heterogeneous structure of their deep-mantle source? Earth Planet. Sci. Lett. 434, 10–17. https://doi.org/10.1016/j.epsl.2015.11.016.

Kaminsky, F., 2018. Water in the Earth’s lower mantle. Geochem. Int. 56, 1117–1134. https://doi.org/10.1134/S0016702918120042.

Karato, S.I., 2013. Theory of isotope diffusion in a material with multiple species and its implications for hydrogen-enhanced electrical conductivity in olivine. Phys. Earth Planet. Inter. 219, 49–54. https://doi.org/10.1016/j.pepi.2013.03.001.

Karlsen, K.S., Conrad, C.P., Magni, V., 2019. Deep water cycling and sea level change since the breakup of Pangea. Geochem. Geophys. Geosyst. 20, 2919–2935. https://doi.org/10.1029/2019GC008232.

van Keken, P.E., Hacker, B.R., Syracuse, E.M., Abers, G.A., 2011. Subduction factory: 4. Depth-dependent flux of H_2O from subducting slabs worldwide. J. Geophys. Res., Solid Earth 116, B01401. https://doi.org/10.1029/2010JB007922.

Kim, T., O’Rourke, J.G., Lee, J., Chariton, S., Prakapenka, V., Husband, R.J., Giordano, N., Liermann, H.P., Shim, S.H., Lee, Y., 2023. A hydrogen-enriched layer in the topmost outer core sourced from deeply subducted water. Nat. Geosci. 16, 1208–1214. https://doi.org/10.1038/s41561-023-01324-x.

Kiraly, A., Portner, D.E., Haynie, K.L., Chilson-Parks, B.H., Gosh, T., Jadamec, M., Makushkina, A., Manga, M., Moresi, L., O’Farrel, K.A., 2020. The effect of slab gaps on subduction dynamics and mantle upwelling. Tectonphysics 785, 228458. https://doi.org/10.1016/j.tecto.2020.228458.

Kohlstedt, D., Kepler, H., Rubie, D.C., 1996. Solubility of water in the α, β and γ phases of $(Mg, Fe)_2SiO_4$. Contrib. Mineral. Petrol. 124, 345–357. https://doi.org/10.1007/s004100050161.

Kohlstedt, D.L., Mackwell, S.J., 1998. Diffusion of hydrogen and intrinsic point defects in olivine. Z. Phys. Chem. 207, 147–162. https://doi.org/10.1524/zpch.1998.207.Part_1_2.147.

Korenaga, J., 2011. Thermal evolution with a hydrating mantle and the initiation of plate tectonics in the early Earth. J. Geophys. Res. 116, B12403. https://doi.org/10.1029/2011JB008410.

Korenaga, J., Planavsky, N.J., Evans, D.A.D., 2017. Global water cycle and the coevolution of the Earth’s interior and surface environment. Philos. Trans. R. Soc. A 375, 20150393. https://doi.org/10.1098/rsta.2015.0393.

Kresse, G., Hafner, J., 1993. Ab initio molecular dynamics for liquid metals. Phys. Rev. B 47, 558. https://doi.org/10.1103/PhysRevB.47.558.

Kresse, G., Joubert, D., 1999. From ultrasoft pseudopotentials to the projector augmented-wave method. Phys. Rev. B 59, 1758–1775. https://doi.org/10.1103/PhysRevB.59.1758.

Labrosse, S., Hernlund, J., Coltice, N., 2007. A crystallizing dense magma ocean at the base of the Earth’s mantle. Nature 450, 866–869. https://doi.org/10.1038/nature06355.

Li, Y., Guo, X., Vočadlo, L., Brodholt, J.P., Ni, H., 2022a. The effect of water on the outer core transport properties. Phys. Earth Planet. Inter. 329–330, 106907. https://doi.org/10.1016/j.pepi.2022.106907.

Li, Y., Vŏcadlo, L., Sun, T., Brodholt, J.P., 2022b. Primitive noble gases sampled from ocean island basalts cannot be from the Earth’s core. Nat. Geosci. 13, 3770. https://doi.org/10.1038/s41467-022-31588-7.

Litasov, K., Ohtani, E., Langenhorst, F., Yurimota, H., Kubo, T., Kondo, T., 2003. Water solubility in Mg-perovskites and water storage capacity in the lower mantle. Earth Planet. Sci. Lett. 211, 189–203. https://doi.org/10.1016/S0012-821X(03)00200-0.

Liu, Z., Fei, H., Chen, L., McCammon, C., Wang, L., Liu, R., Wang, F., Liu, B., Katsura, T., 2021. Bridgmanite is nearly dry at the top of the lower mantle. Earth Planet. Sci. Lett. 570. https://doi.org/10.1016/j.epsl.2021.117088.

Liu, Z., Ishii, T., Katsura, T., 2017. Rapid decrease of $MgAlO_{2.5}$ component in bridgmanite with pressure. Geochem. Perspect. Lett. 5, 12–18. https://doi.org/10.7185/geochemlet.1739.

Mackwell, S.J., Kohlstedt, D.L., 1990. Diffusion of hydrogen in olivine: implications for water in the mantle. J. Geophys. Res. 95, 5079. https://doi.org/10.1029/JB095iB04p05079.

Manga, M., 1996. Mixing of heterogeneities in the mantle: effect of viscosity differences. Geophys. Res. Lett. 23, 403–406. https://doi.org/10.1029/96GL00242.

Manthilake, G.M., de Koker, N., Frost, D.J., McCammon, C.A., 2011. Lattice thermal conductivity of lower mantle minerals and heat flux from Earth's core. Proc. Natl. Acad. Sci. 108, 17901–17904. https://doi.org/10.1073/pnas.1110594108.

Mao, H.K., Hu, Q.Y., Yang, L.X., 2017. When water meets iron at Earth's core–mantle boundary. Natl. Sci. Rev. 4, 870–878. https://doi.org/10.1093/nsr/nwx109.

McCammon, C., 1997. Perovskite as a possible sink for ferric iron in the lower mantle. Nature 387, 694–696. https://doi.org/10.1038/42685.

van der Meer, G.D., Spakman, W., van Hinsbergen, D.J.J., Amaru, M.L., Torsvik, T.H., 2010. Towards absolute plate motions constrained by lower-mantle slab remnants. Nat. Geosci. 3, 36–46. https://doi.org/10.1038/ngeo708.

van der Meer, D.G., van Hinsebergen, D.J.J., Spakman, W., 2018. Atlas of the underworld: slab remnants in the mantle, their sinking history, and a new outlook on lower mantle viscosity. Tectonophysics 723, 309–448. https://doi.org/10.1016/j.tecto.2017.10.004.

Mohn, C.E., Krynski, M., Kob, W., Allan, N.L., 2021. Cooperative excitations in superionic PbF_2. Philos. Trans. R. Soc. A 379, 20190455. https://doi.org/10.1098/rsta.2019.0455.

Mohn, C.E., Stølen, S., Hull, S., 2009a. Diffusion within α-CuI studied using ab initio molecular dynamics simulations. J. Phys. Condens. Matter 21, 335403. https://doi.org/10.1088/0953-8984/21/33/335403.

Mohn, C.E., Stølen, S., Norberg, S.T., Hull, S., 2009b. Oxide-ion disorder within the high temperature δ phase of Bi_2O_3. Phys. Rev. Lett. 102, 155502. https://doi.org/10.1103/PhysRevLett.102.155502.

Mohn, C.E., Trønnes, R., 2016. Iron spin state and site distribution in $FeAlO_3$-bearing bridgmanite. Earth Planet. Sci. Lett. 440, 178–186. https://doi.org/10.1016/j.epsl.2016.02.010.

Muir, J.M.R., Brodholt, J.P., 2018. Water distribution in the lower mantle: implications for hydrolytic weakening. Earth Planet. Sci. Lett. 484, 363–369. https://doi.org/10.1016/j.epsl.2017.11.051.

Murakami, M., Hirose, K., Yurimoto, H., Nakashima, S., Takafuji, N., 2002. Water in Earth's lower mantle. Science 295, 1885–1887. https://doi.org/10.1126/science.1065998.

Nishi, M., Irifune, T., Tsuchiya, J., Tange, Y., Nishihara, Y., Fujino, K., Higo, Y., 2014. Stability of hydrous silicate at high pressures and water transport to the deep lower mantle. Nat. Geosci. 7, 224–227. https://doi.org/10.1038/ngeo2074.

Ohta, K., Yagi, T., Taketoshi, N., Hirose, K., Komabayashi, T., Baba, T., Ohishi, Y., Hernlund, J., 2012. Lattice thermal conductivity of $MgSiO_3$ perovskite and post-perovskite at the core–mantle boundary. Earth Planet. Sci. Lett. 349–350, 109–115. https://doi.org/10.1016/j.epsl.2012.06.043.

Ohtani, E., Zhao, D., 2009. The role of water in the deep upper mantle and transition zone: dehydration of stagnant slabs and its effects on the big mantle wedge. Russ. Geol. Geophys. 50, 1073–1078. https://doi.org/10.1016/j.rgg.2009.11.006.

Okuda, Y., Ohta, K., Hasegawa, A., Yagi, T., Hirose, K., Kawaguchi, S.I., Ohishi, Y., 2020. Thermal conductivity of Fe-bearing post-perovskite in the Earth's lowermost mantle. Earth Planet. Sci. Lett. 547, 116466. https://doi.org/10.1016/j.epsl.2020.116466.

Okuda, Y., Ohta, K., Yagi, T., Sinmyo, R., Wakamatsu, T., Hirose, K., Ohishi, Y., 2017. The effect of iron and aluminum incorporation on lattice thermal conductivity of bridgmanite at the Earth's lower mantle. Earth Planet. Sci. Lett. 474, 25–31. https://doi.org/10.1016/j.epsl.2017.06.022.

Panero, W.R., Caracas, R., 2020. Stability and solid solutions of hydrous alumino-silicates in the Earth's mantle. Minerals 10, 330. https://doi.org/10.3390/min10040330.

Parai, R., Mukhopadhyay, S., 2012. How large is the subducted water flux? New constraints on mantle regassing rates. Earth Planet. Sci. Lett. 317–318, 396–406. https://doi.org/10.1016/j.epsl.2011.11.024.

Pearson, D.G., Bremker, F.E., Nestola, F., McNeill, J., Nasdala, L., Hutchison, M.T., Matveev, S., Mather, K., Silversmit, G., Schmitz, S., Vekemans, B., Vincze, L., 2014. Hydrous mantle transition zone indicated by ringwoodite included within diamond. Nature 507, 221–223. https://doi.org/10.1038/nature13080.

Peng, Y., Deng, J., 2024. Hydrogen diffusion in the lower mantle revealed by machine learning potentials. J. Geophys. Res., Solid Earth 129, e2023JB028333. https://doi.org/10.1029/2023JB028333.

Perdew, J.P., Burke, K., Ernzerhof, M., 1996. Generalized gradient approximation made simple. Phys. Rev. Lett. 77, 3865. https://doi.org/10.1103/PhysRevLett.77.3865.

Peslier, A.H., Schönbächler, M., Busemann, H., Karato, S.I., 2017. Water in the Earth's interior: distribution and origin. Space Sci. Rev. 212, 743–810. https://doi.org/10.1007/s11214-017-0387-z.

Rudolph, M.L., Lekić, V., Lithgow-Bertelloni, C., 2015. Viscosity jump in Earth's mid-mantle. Science 350, 1349–1352. https://doi.org/10.1126/science.aad1929.

Rüpke, L.H., Morgan, J.P., Hort, M., Connolly, J.A.D., 2004. Serpentine and the subduction zone water cycle. Earth Planet. Sci. Lett. 223, 17–34. https://doi.org/10.1016/j.epsl.2004.04.018.

Sandu, C., Lenardic, A., McGovern, P., 2011. The effects of deep water cycling on planetary thermal evolution. J. Geophys. Res. 116, B12404. https://doi.org/10.1029/2011JB008405.

Schaefer, L., Fegley, B., 2010. Chemistry of atmospheres formed during accretion of the Earth and other terrestrial planets. Icarus 208, 438–448. https://doi.org/10.1016/j.icarus.2010.01.026.

Schmandt, B., Jacobsen, S.D., Becker, T.W., Liu, Z., Dueker, K.G., 2014. Dehydration melting at the top of the lower mantle. Sciences 344, 1265–1268. https://doi.org/10.1126/science.1253358.

Shankland, T.J., Peyronneau, J., Poirier, J.P., 1993. Electrical conductivity of the Earth's lower mantle. Nature 366, 453–455. https://doi.org/10.1038/366453a0.

Solomatov, V., El-Khozondar, R., Tikare, V., 2002. Grain size in the lower mantle: constraints from numerical modeling of grain growth in two-phase systems. Phys. Earth Planet. Inter. 129, 265–282. https://doi.org/10.1016/S0031-9201(01)00295-3.

Stixrude, L., Karki, B., 2005. Structure and freezing of $MgSiO_3$ liquid in Earth's lower mantle. Science 310, 297–299. https://doi.org/10.1126/science.1116952.

Stixrude, L., de Koker, N., Sun, N., Mookherjee, M., Karki, B.B., 2009. Thermodynamics of silicate liquids in the deep Earth. Earth Planet. Sci. Lett. 278, 226–232. https://doi.org/10.1016/j.epsl.2008.12.006.

Sun, W., Yoshino, T., Sakamoto, N., 2015. Hydrogen self-diffusivity in single crystal ringwoodite: implications for water content and distribution in the mantle transition zone. Geophys. Res. Lett. 42, 6582–6589. https://doi.org/10.1002/2015GL064486.

Torsvik, T.H., Steinberger, B., Ashwal, L.D., Doubrovine, P.V., Tronnes, R.G., 2016. Earth evolution and dynamics – a tribute to Kevin Burke. Can. J. Earth Sci. 53, 1073–1087. https://doi.org/10.1139/cjes-2015-0228.

Trønnes, R.G., Barona, M.A., Eigenmann, K.R., Guren, M.G., Heyn, B.H., Løken, A., Mohn, C.E., 2019. Core formation, mantle differentiation and core-mantle interaction within Earth and the terrestrial planets. Tectonophysics 760, 165–198. https://doi.org/10.1016/j.tecto.2018.10.021.

Van Orman, J.A., Krawczynski, M.J., 2015. Theoretical constraints on the isotope effect for diffusion in minerals. Geochim. Cosmochim. Acta 164, 365–381. https://doi.org/10.1016/j.gca.2015.04.051.

Walter, M., 2021. Water transport to the core–mantle boundary. Natl. Sci. Rev. 8, 1–4. https://doi.org/10.1093/nsr/nwab007.

Wu, J., Desch, S.J., Schaefer, L., Elkins-Tanton, L.T., Pahlevan, K., Buseck, P.R., 2018. Origin of Earth's water: chondritic inheritance plus nebular ingassing and storage of hydrogen in the core. J. Geophys. Res., Solid Earth 123, 2691–2711. https://doi.org/10.1029/2018JE005698.

Yoshino, T., 2019. Penetration of molten iron alloy into the lower mantle phase. C. R. Géosci. 351, 171–181. https://doi.org/10.1016/j.crte.2018.06.013.

Yoshino, T., Kamada, S., Zhao, C., Ohtani, E., Hirao, N., 2016. Electrical conductivity model of Al-bearing bridgmanite with implications for the electrical structure of the Earth's lower mantle. Earth Planet. Sci. Lett. 434, 208–219. https://doi.org/10.1016/j.epsl.2015.11.032.

Yoshino, T., Manthilake, G., Matsuzaki, T., Katsura, T., 2008. Dry mantle transition zone inferred from the conductivity of wadsleyite and ringwoodite. Nature 451, 326–329. https://doi.org/10.1038/nature06427.